Resolving Jahn-Teller induced vibronic fine structure of silicon vacancy quantum emission in silicon carbide

Marianne Etzelmüller Bathen, Augustinas Galeckas, Robert Karsthof, Aymeric Delteil, Vincent Sallet, Andrej Yu. Kuznetsov, Lasse Vines

Resolving Jahn-Teller induced vibronic fine structure of silicon vacancy quantum emission in silicon carbide

Marianne Etzelmüller Bathen,[1,2,*] Augustinas Galeckas,[2] Robert Karsthof,[2]
Aymeric Delteil,[3] Vincent Sallet,[3] Andrej Yu. Kuznetsov,[2] and Lasse Vines[2]

[1]*Advanced Power Semiconductor Laboratory, ETH Zürich, Physikstrasse 3, 8092 Zürich, Switzerland*
[2]*Department of Physics/ Centre for Materials Science and Nanotechnology, University of Oslo, N-0316 Oslo, Norway*
[3]*Université Paris-Saclay, UVSQ, CNRS, GEMaC, 78000, Versailles, France*

(Dated: June 24, 2021)

Point defects in semiconductors are promising single-photon emitters (SPEs) for quantum computing, communication and sensing applications. However, factors such as emission brightness, purity and indistinguishability are limited by interactions between localized defect states and the surrounding environment. Therefore, it is important to map the full emission spectrum from each SPE, to understand the complex interplay between the different defect configurations, their surroundings and external perturbations. Herein, we investigate a family of regularly spaced sharp luminescence peaks appearing in the near-infrared portion of photoluminescence (PL) spectra from n-type 4H-SiC samples after irradiation. This periodic emitter family, labeled the L-lines, is only observed when the zero-phonon line signatures of the negatively charged Si vacancy (so-called V-lines) are present. The L-lines appear with 1.45 meV and 1.59 meV energy spacing after H and He irradiation and increase linearly in intensity with fluence — reminiscent of the intrinsic defect trend. Furthermore, we monitor the dependence of the L-line emission energy and intensity on heat treatments, electric field strength and PL collection temperature, discussing these data in the context of the L-lines. Based on the strong similarity between the irradiation, electric field and thermal responses of the L- and V-lines, the L-lines are attributed to the Si vacancy in 4H-SiC. The regular and periodic appearance of the L-lines provides strong arguments for a vibronic origin explaining the oscillatory multi-peak spectrum. To account for the small energy separation of the L-lines, we propose a model based on rotations of distortion surrounding the Si vacancy driven by a dynamic Jahn-Teller effect.

I. INTRODUCTION

Silicon carbide is a versatile material with application areas ranging from power electronics to quantum technology [1,2]. As a host material for quantum devices, SiC harbors a plethora of point defects exhibiting single-photon emission, long spin coherence times and coherent spin manipulation, even at room temperature. By exploiting localized spin control, the quantum defect centers can be employed as qubits via gate operations to isolated spins, while single-photon emitters (SPEs) find wide-spread use for, e.g., spin-photon entanglement and quantum cryptography. Promising quantum contenders in 4H-SiC include the silicon vacancy [3,4] and various complexes thereof [5–7], with transition metal impurities recently gaining more attention [8].

The Si vacancy (V_{Si}) in 4H-SiC is a SPE in the near-infrared (NIR) portion of the spectrum. The negative charge state of V_{Si}, V_{Si}^{-}, exhibits three zero-phonon lines (ZPLs) called the V-lines: V1′, V1 and V2, at 858 nm, 861 nm and 916 nm, respectively [3,9,10]. V1 and V1′ have been attributed to different excited states of V_{Si}^{-} at a hexagonal (h) lattice site, while V2 arises from the pseudo-cubic $V_{\mathrm{Si}}^{-}(k)$ [11]. Emission related to the second excited state of $V_{\mathrm{Si}}^{-}(k)$, V2′, has been theorized [12–14] but not detected. Although the V_{Si} is a high-fidelity SPE with a relatively large portion of the emitted light being channeled into the ZPL (Debye-Waller factor ∼8-9 %) [12,15–17] compared to, e.g., the nitrogen-vacancy (NV) center in diamond, it is vital to understand the influence of environmental effects on the V_{Si} emission spectrum. Indeed, emission from V_{Si} (and comparable color centers) is often afflicted by inhomogeneous broadening arising from local strain and stray electric fields, reducing the emission purity, indistinguishability and brightness. See, e.g., Ref. [18] for further discussion on this matter.

To successfully employ V_{Si} and other SPEs in SiC for quantum applications, control over emission energies must be gained, both to circumvent any undesired influence from the environment and to tailor the photon energy specifically for each application. Several advances in this regard have already been made, motivated by attaining indistinguishable photons for, e.g., secure quantum networks and entanglement protocols. Controlled and reliable formation of Si vacancies has been studied based on, e.g., proton beam writing [19], focused ion implantation to form scalable defect arrays [20,21], and femtosecond laser writing [22]. Electric fields offer promising means of manipulating and controlling SPEs, as demonstrated by recent studies on spectral tuning of the V_{Si} [23–25] and divacancy ($V_{\mathrm{Si}}V_{\mathrm{C}}$) [26–28] via the Stark effect [29]. Notably, it was recently proposed [12] and shown [30] that also the local inhomogeneties modifying emission energies can be exploited, by embedding V_{Si} defects in SiC micro-and nanoparticles of predominantly the 6H polytype. While Stark effect tuning yielded V_{Si} (in 4H-SiC) emission shifts of 1-3 meV [23,24], strain effects may correspondingly cause emission tuning of the characteristic V_{Si} ZPLs (in 6H-SiC) of up to 26 meV [30]. Nevertheless, an advanced understanding of the interplay between SPEs, their local environment and external perturbation is vital for the successful integration of the V_{Si} and comparable quantum emitters with devices.

Theoretical methods are useful for assigning zero-

* bathen@aps.ee.ethz.ch

phonon line energies to specific defect centers (see, e.g., Ref. [31]), and for analyzing the full emission lineshape including the phonon side-band (PSB) (see, e.g., Ref. [32]). For instance, a recent theoretical work evaluated the closest local vibrational mode at approximately 36 meV away from the V2 ZPL [33], while the calculations of Ref. [14] corroborated that the PSBs are separated from the V1, V1′, V2 and V2′ ZPLs by at least 30 meV. Furthermore, the V1′ and V2′ excited states were predicted to be polaronic as opposed to electronic [12], due to strong coupling of the localized electron states to lattice vibrations.

The predicted polaronic nature of the V_{Si}^{-} second excited states [12] indicates that electron-phonon coupling plays a prominent role in the excitation process, and may be responsible for emission fine structure beyond the classical phonon modes. Furthermore, V1′ and V2′ are orbitally degenerate [11,12,34], leaving the excited states of V_{Si}^{-} vulnerable to a symmetry-lowering Jahn-Teller distortion. Experimental [16,35] and theoretical [36] works have previously inferred and predicted that Jahn-Teller effects may be affecting luminescence and spin signals from the V_{Si}, but no direct observations of luminescence line splitting effects have so far been made. Accordingly, further work is needed to illuminate the complex interplay between quantum emission and electron-phonon coupling in the case of quantum compatible defects in 4H-SiC.

Multiple studies have investigated the NIR portions of the 4H-SiC emission spectrum from samples of both p-, n- and intrinsic type (see, e.g., Refs. [9,10,37,38]). However, a number of spectral features remain unexplored and corresponding identification is missing. Herein, we investigate a family of narrow peaks appearing in photoluminescence (PL) spectra of proton irradiated 4H-SiC samples (labeled the L-lines) that emerge close to the V1 and V1′ emission lines arising from the $V_{\mathrm{Si}}^{-}(h)$. Note that two of the L-lines, L1 and L2, were shown but not discussed in Ref. [38]. We report on formation conditions, excitation properties, electric field dependence and thermal response of the L-lines, and discuss their possible origins. The results give ample support for a tentative assignment of the L-lines to the V_{Si}, and we further argue for a vibronic origin related to rotational (or electronic bond-switching) effects. The dynamic Jahn-Teller effect is suggested to be responsible for decreasing the vibronic energy separations for the L-lines.

II. METHODS

Emission from n-type 4H-SiC was studied using samples having 10 µm epitaxial layers and showing the (0001)-plane (or c-face) that were purchased from Cree, Inc. The epi-layers were n-doped (nitrogen) with net carrier concentrations of $N_{\mathrm{D}}{\sim}1 \cdot 10^{15}$ cm^{-3} as determined by capacitance-voltage (CV) measurements, and the substrates were n-doped to approximately $8 \cdot 10^{18}$ cm^{-3}. Primary point defects were created by ion implantation or irradiation via three different approaches. One set of samples (labeled H-irradiated) were irradiated with 1.8 MeV protons to fluences in the range $1 \cdot 10^{12}$ cm^{-2} to $8 \cdot 10^{13}$ cm^{-2}, having a projected range of about 27 µm calculated by collision Monte Carlo models as manifested in the SRIM (Stopping and Range for Ions in Matter) code [39]. The second sample set (He-implanted) was implanted with either 2.7 MeV He ions to a fluence of $1.6 \cdot 10^{12}$ cm^{-2} (projected range of ∼6.7 µm), or with 300 keV He ions to a fluence of $1.6 \cdot 10^{11}$ cm^{-2} (projected range of 900 nm). The different implantation procedures resulted in two different sample types: one where a Gaussian-like distribution of implantation-induced defects resides within the near-surface region of the sample (He-implanted), and one where the defect distribution remains approximately uniform throughout the epi-layer (H-irradiated). All irradiation and implantation procedures were performed at room temperature and with the samples tilted 8 ° off with respect to the sample's surface normal to diminish channeling effects. Following the implantation procedure, all samples were annealed at 300 °C in nitrogen flow for 30 minutes to alleviate implantation damage and remove unwanted non-radiative channels, for instance by interstitial defects. Subsequent heat treatments were conducted at 400 °C, 600 °C and 800 °C in nitrogen flow for 30 minutes on selected samples to reveal the annealing behavior of the L-line defect(s) in relation to that of the V_{Si}. A conventional tube furnace was employed for all heat treatments.

For the photoluminescence spectroscopy, the samples were placed inside a closed-cycle He refrigerator system (CCS-450 Janis Research, Inc.). PL measurements were conducted at temperatures ranging from 10 K to 300 K. Photoexcitation was performed using either continuous wave (cw) lasers having excitation wavelengths of 405 nm or 806 nm, or a pulsed Ti:sapphire tunable laser operating in femtosecond mode-locked mode for resonant excitation of the NIR emitters (V-lines and L-lines) at a wavelength of 740 nm. In all cases, the focused laser beam was impinging on the sample surface at 27 ° and yielded polarization perpendicular to the optic (c) axis of 4H-SiC. The emission was analyzed by fiber-optic (Ocean Optics, HR4000) and imaging spectrometer systems (Horiba iHR320 coupled to Andor iXon888 EMCCD), with a spectral resolution below 0.2 nm in both cases. The imaging spectroscopy setup ensured near-confocal operation, allowing to maximize the collection of emission from depths of ∼5 µm below the epi-layer surface without probing the stopping range regions of implanted hydrogen (in the case of H-irradiated samples). Spatial PL maps (300 keV He implantation) confirm that the L-lines are heterogeneously distributed across the sample after irradiation. A spectral map further demonstrated that the L1 and L2 lines are not found everywhere, and that their positions are not necessarily correlated (see Supplemental Material at [40] for spectral maps of the L- and V-lines).

The electric field dependence of the NIR emission was investigated using the same measurement setup and sample geometry as in Ref. [23]. Schottky barrier diodes (SBDs) with 150 nm thickness and 1 mm diameter Ni contacts were formed on the 4H-SiC epi-layer surface using electron beam evaporation through a shadow mask, to facilitate application of varying electric fields by biasing the SBD. The samples employed for the electric field studies had first been proton-irradiated to fluences of $1 \cdot 10^{12}$ cm^{-2} or $2 \cdot 10^{12}$ cm^{-2}. The maximum electric field strength (ξ_{m}) resulting from the presence of the Schottky barrier

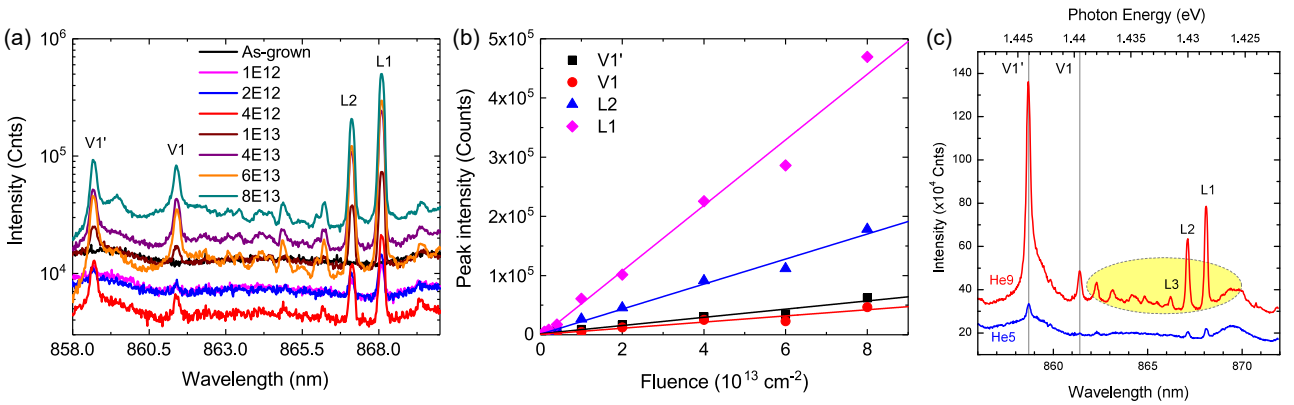

FIG. 1. Emission collected at 10 K from n-type 4H-SiC samples that are (a) as-grown (black) and proton-irradiated to fluences ranging from $1 \cdot 10^{12}$ cm^{-2} to $8 \cdot 10^{13}$ cm^{-2}, with (b) showing the proton fluence dependence of the background-subtracted emission intensities of V1/V1' (related to the Si vacancy) and L1/L2. Excitation was performed using a 740 nm tunable laser. Panel (c) shows the V1/V1′ and L-lines in He-implanted samples. He implantation was performed at an energy of 300 keV (He5, blue) or 2.7 MeV (He9, red). Excitation was performed using a 405 nm cw laser.

combined with applied bias depends on the depletion region width (W) according to $\xi_{\rm m} = -(q/\epsilon)N_{\rm D}W$, where $W = \sqrt{2\epsilon(V_{\rm bi} - V_{\rm applied})/(qN_{\rm D})}$. Here, $N_{\rm D}$ is the net carrier concentration, q the fundamental charge, ϵ the semiconductor permittivity, $V_{\rm applied}$ is the applied bias and $V_{\rm bi}$ the built-in voltage. From CV measurements we found that $V_{\rm bi} = 1.5$ V with the Schottky barrier height being approximately $\Phi_{\rm B} = 1.7$ V. The depletion region depth was measured to be $\sim$1.5 µm without applied bias, and is extended up to $\sim$4 µm when applying -10 V reverse bias to the SBD. Applying -60 V to the SBD ensures electric field strengths of $\sim$15 MV/m parallel to the surface normal. The dependence of the L-line emission on electric fields was investigated by conducting PL measurements in a back-scattering geometry from the substrate side of the sample (see Ref. [23] for illustration), while otherwise the emission was collected from the epi-layer surface. For the field dependence studies, 740 nm excitation was employed and the focus was situated within the space charge region (SCR) of the Schottky barrer diode.

III. RESULTS

A. Irradiation dependence of NIR emitters

Figure 1 shows the evolution of the PL emission from irradiated n-type 4H-SiC epi-layers in the wavelength range 855-872 nm, i.e., near the V1 and V1′ emission lines arising from $V_{\rm Si}^{-}(h)$ [11], as a function of H and He irradiation. Fig. 1(a) compares the as-grown case (black line) to proton-irradiated samples, revealing the appearance and growth of the V-lines and what will be referred to as L-lines herein (V1, V1′, L1 and L2 are labeled in Fig. 1a). Note that the evolution of V2 ($V_{\rm Si}^{-}$ at k site) was not studied in this work, because the overlap between V2 and the broad $V_{\rm Si}$-related phonon side-band obscures the fine structure near the V2 zero-phonon line.

While the two most dominant of the L-peaks, L1 and L2, are visible even for the lowest proton fluence ($1 \cdot 10^{12}$ cm^{-2}), the weaker L-line components are challenging to distinguish for proton fluences below $8 \cdot 10^{13}$ cm^{-2}. Interestingly, both L1 and L2 increase linearly with the proton fluence, as demonstrated by the background-subtracted emission intensities shown in Fig. 1(b). However, L1 and L2 do not share the same slope, as is the case for V1 and V1′, and the linearities of both L-lines deviate from that of the V-lines (V1 and V1′). The linear fluence dependencies of L1 and L2 emphasize the likelihood of an intrinsic and primary origin such as a vacancy or an interstitial defect, especially upon comparing to V1 and V1′. Another important feature of the L-lines is that they appear regardless of whether H or He ions are used for irradiation, as demonstrated by Fig. 1(c), evidencing that the emission is likely not hydrogen-related but rather of intrinsic origin.

Overall, the less intense L-lines (L3-L7) are more distinguishable after He implantation as compared to proton irradiation (see yellow color marked region in Fig. 1c). We cannot exclude that this is at least partly related to hydrogen acting as a passivating agent for the defects responsible for emission, and effectively quenching the V- and/or L-lines (see, e.g., Ref. [41] for a discussion on the interplay between H and $V_{\rm Si}$ in 4H-SiC). Interestingly, the L1/L2 peak intensities are larger than those of V1/V1′ for the 740 nm excitation wavelength used in Fig. 1(a) (also for 806 nm excitation, not shown). However, the roles are reversed when a 405 nm cw-laser is used as exemplified in Fig. 1(c). Importantly, this trend holds for different laser power densities and regardless of whether H or He irradiation was employed (not shown). Accordingly, we cannot extract any reliable information regarding the concentration of the L-line defect center(s) in relation to that of the V-lines on the basis of the PL intensities. We will return to the issue of excitation dependence below.

Spectral maps shown in the Supplemental Material (see Supplementary Figures S2 and S3 at [40]) reveal that the V1, L1 and L2 lines are heterogeneously distributed in the He-implanted (300 keV) sample. Moreover, the presence

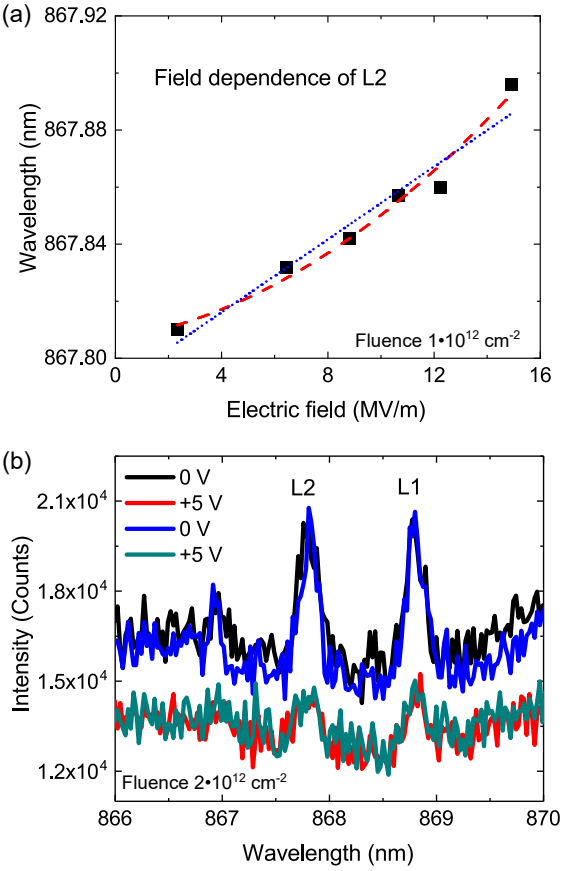

FIG. 2. Electric field dependence of the L1 and L2 lines in 4H-SiC samples that were proton-irradiated to fluences of $1 \cdot 10^{12}$ cm^{-2} (a) or $2 \cdot 10^{12}$ cm^{-2} (b); notably, panel (a) reveals a prominent Stark shift for L2 of either linear (blue dotted line) or weakly quadratic (red dashed line) character. Note that the L1 position remains unaffected for all applied voltages (remaining L-lines are below detection limit). Intensity modulation of L1 and L2 by biasing a Schottky barrier diode (SBD) is shown in (b) for a $+5$ V forward bias. All electric field measurements were conducted using 740 nm excitation, with the Stark shift collected at 50 K and modulation at 10 K.

of L1 and L2 appear not to be correlated. On the other hand, as shown by PL spectra collected from different locations a few μm apart in Supplementary Figure S4, L1 can appear without (or with weak) L2, but L2 is only seen when L1 is present.

B. Influence of electric field

The electric field dependence of the V_{Si} emission lines has been investigated in some detail previously; both pronounced Stark shifts for the V1′ and V1 lines [23, 24] and emission intensity modulation evidencing charge-state switching of V_{Si} [23,42] have been demonstrated. The electric field responses of the dominant L-lines (L1 and L2) were studied at cryogenic temperatures (10 K and 50 K) for proton-irradiated 4H-SiC samples, and are summarized in Figure 2. Firstly, it is important to note that the L-lines are clearly visible both when collecting the luminescence from the epi-layer surface, as shown in Fig. 1, and for the SBD–epitaxial layer–substrate geometry employed in the electric field dependence studies. This, along with the presence of the L-lines irrespective of excitation mode (cw or pulsed laser), discounts any measurement artifacts as being responsible for the L-lines. Secondly, the presence of SBDs on the 4H-SiC epi-layer surface, and the resulting electric field, appears to significantly enhance the L-line intensity as compared to the SBD-free case. This was demonstrated, but not discussed, in Ref. [23] (see Supplemental Material at [40] for illustration). Indeed, within the depletion region beneath a Schottky diode, the L-lines increase in a similar fashion as V1′, but the trend is somewhat weaker. Note that the V1 ZPL was barely observed beneath the SBD.

Monitoring the wavelengths of L1 and L2 versus electric field strength reveals that, intriguingly, L2 shifts with the applied field while L1 does not (see Fig. 2a for L2, L1 not shown). The different electric field responses of the L1 and L2 lines indicate that the L-lines must arise from at least two different interactions, however might still be closely related bearing in mind the similarities in their generation behaviors in Fig. 1. Importantly, the observed Stark effect for L2 suggests a connection between L2 and the V_{Si}-related emission lines. A pronounced quadratic Stark effect was found for V1′ when $\xi \parallel c$ in Refs. [23,24], while V1 exhibited a near-linear field response for the same case [24]. Note that the Stark tuning behavior is expected to depend strongly on the direction of the applied electric field, as reported for V1 and V1′ in Ref. [24]. The field dependence of the L2 wavelength may be well captured by both linear and weakly quadratic fits (see Fig. 2a), complicating its unique assignment to either V1 or V1′. Nonetheless, the applied field induces a small red-shift for both L2 and V1′ [23], while V1 shifts in the opposite direction when $\xi \parallel c$ [24]. Note that the size of the Stark shift for L2, of $\sim$1 meV, is similar to, albeit smaller than, that found for V1′ in a comparable sample type ($\sim$3 meV [23]).

Sequential modulation of the L1 and L2 emission intensities is achieved by cycled switching to a forward ($+5$ V, see Fig. 2b) or reverse (see Supplemental Material at [40] for intensity switching at -2 V) bias to the SBD. We reveal that the peak intensities of L1 and L2 can be sequentially suppressed at 10 K upon application and removal of a forward or reverse bias, similarly to that found for the V_{Si}-related V1′ ZPL in Ref. [23]. The repeated intensity quenching observed for L1 and L2 indicates that charge-state switching is occurring for both V_{Si} and the L-line defect(s). The quenching of the L-lines with reverse or large forward ($>$ 1.5 V) bias is reproducible for different samples and proton fluences, and is visible also for L3 in samples with higher defect concentrations. Extending the comparison to the charge-state switching shown for V_{Si} ensembles [23], we also reproduce the enhancement of emission intensities for L1 and L2 that was found for V1′ when employing a $+1$ V forward bias (not shown). Importantly, the field effect is independent of defect concentration and observable for the L-lines even in the dilute limit with $\sim 10^{13}$ cm^{-3} vacancy defects (Fig. 2), reinforcing the notion that the L-peak appearance is a localized effect. Together, these observations point towards a shared origin between V1/V1′ (i.e., the negatively charged V_{Si}) and the L-lines.

C. Thermal response

Figure 3 summarizes the thermal stability of V1, V1′, L1 and L2 in a proton-irradiated sample (fluence of $4 \cdot 10^{13}$ cm^{-2}) upon anneals at 300-800 °C. Importantly, both L1 and L2 are enhanced or retain their intensity upon annealing at 400 °C as compared to that for 300 °C, correlating with the thermal response of V1 and V1′ assigned to V_{Si}^{-}. Thereafter, the L-lines are substantially quenched upon 600 °C annealing and vanish at ≥800 °C. In contrast, the V_{Si} remains visible for the high temperature annealing conditions, as evidenced by the presence of V1 and V1′ in the sample annealed at 800 °C. It is important to note at this point that the apparent disappearance of the L-lines while V1 and V1′ remain detectable in Fig. 3 is influenced by the fact mentioned earlier that excitation at 405 nm wavelength strongly affects the strength relation between the V- and L-lines, favoring the former.

A comparison of the background-subtracted peak intensities for the V1, V1′, L1 and L2 lines is presented in the Supplemental Material (see Figure S7 at [40]) as a function of annealing temperature for different proton irradiation fluences. In short, the qualitative thermal responses of the L- and V-lines are similar, with an intensity reduction above 600 °C. A quantitative analysis is challenging due to the strong dependence of emission intensity on excitation photon energy discussed above. Importantly, V_{Si} is associated with high formation energies [23,43] and cannot be formed thermally for the temperatures used in Fig. 3. Therefore, the enhanced V1′ emission intensities upon increasing the annealing temperature from 300 °C to 400 °C cannot be explained by an increase in V_{Si} concentration. A more likely explanation related to a reduction of non-radiative channels due to out-annealing of implantation damage must therefore be considered (see, e.g., Ref. [44] for a related discussion). The different responses of V1 and V1′ to temperature (see Supplemental Material at [40] for detailed illustration with background subtraction), on the other hand, are more challenging to explain according to this theory.

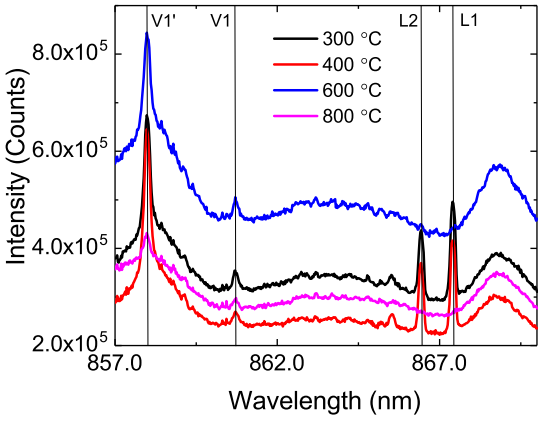

FIG. 3. Evolution of the L- and L-lines as a function of annealing temperature in the range 300-800 °C for the proton-irradiated sample to a fluence $4 \cdot 10^{13}$ cm^{-2}. The PL spectra were obtained at 10 K using a 405 nm cw laser as an excitation source.

Further insights into the origin of the multi-lines can be attained from the thermal evolution of the individual peaks, which is depicted in Figure 4(a) for a proton-irradiated sample (fluence $8 \cdot 10^{13}$ cm^{-2}) in the temperature range 10-300 K. Firstly, we observe that the weaker L-lines apparently vanish above 50 K, while the most intense ones (L1 and L2) remain visible up to 100 K. All traces of the L-lines have disappeared at 150 K and above, while emission related to V_{Si} can be distinguished (albeit broadened) even at room temperature [4].

The integrated intensities of the V- and L-lines as a function of temperature are presented in the Arrhenius plots in Figure 4(b), along with numerical fits that enable estimation of the activation energies for thermal quenching. Interestingly, the thermal evolution of different peaks in the same subsets notably differ, exhibiting either stable thermal quenching (TQ) or so-called negative thermal quenching (NTQ) features. Indeed, while steady TQ occurs for V1 and L1, there is first a notable thermal activation for the V1′ and L3 peaks ($E' = -2.8$ meV), and to a lesser extent for L2 and L4 ($E' = -0.7$ meV). At elevated temperatures, all peaks become quenched exhibiting two activation energies for thermal quenching, initially $E1 \sim 10$ meV and ultimately $E2 \sim 75$ meV. Based on the PL(T) dependence of the NIR emission, we again conclude that at least two different origins are needed to explain the L-line behavior. Additionally, we observe complementary thermal activation and quenching behaviors for the V- and L-lines, indicating pairwise relations between (at least) V1 and L1, and V1′ and L3 (with the potential addition of L2 and L4).

IV. ANALYSIS AND DISCUSSION

To summarize, the L-lines discussed herein appear in immediate proximity to the V1 and V1′ ZPLs associated with the negatively charged $V_{Si}(h)$ in 4H-SiC, and have not been observed in the absence of V_{Si}-related emission lines. Importantly, several properties observed for the L-lines indicate a shared origin with that of V1/V1′. Firstly, the L-lines appear after irradiation regardless of ion species (see Figs. 1a and 1c), and increase linearly in emission intensity with proton fluence (Fig. 1b). On the other hand, the slope of the fluence dependence differs between L1 and L2, indicating differences regarding their origin. Additionally, we note that the excitation wavelength strongly influences the relative strength between the L- and V-lines, with the L-lines being weaker than V1/V1′ for higher energy excitation (405 nm) but stronger for, e.g., the 740 nm case. A second point in favor of the L-lines' association with V_{Si} is the electric field dependence (Fig. 2). Intensity enhancement beneath an SBD, Stark shifts and field-dependent intensity modulation are all found for at least one of the L-lines, while individual differences between L1 and L2 corroborate the hypothesis that the L-lines can be sub-divided into at least two groups. The temperature behavior of the V-lines and L-lines also indicates that there is a pairing trend for these lines (see Fig. 4). As a result, the behavior of the L-lines can be grouped into two categories: similar

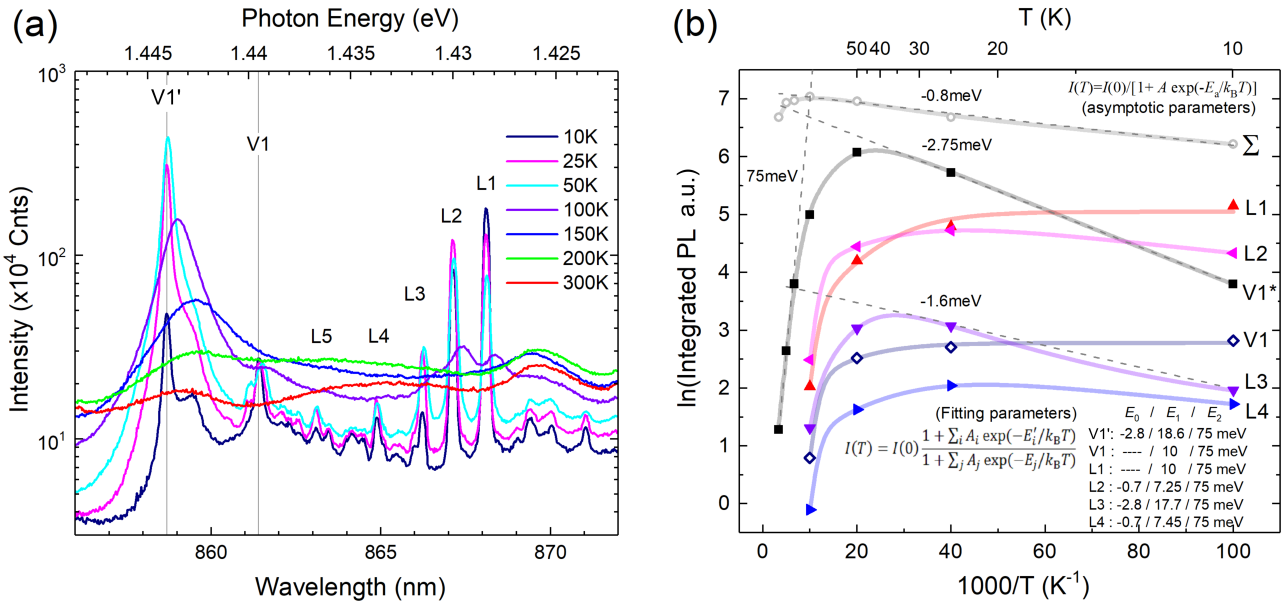

FIG. 4. Dependence of the L-lines on PL collection temperature for a sample irradiated with 1.8 MeV protons to a fluence of $8 \cdot 10^{14}$ cm^{-2}. Panel (a) shows PL spectra as a function of temperature, while (b) displays Arrhenius plots of the key emission components (peaks V1/V1′ and L1-L4) and of the total (integrated) PL intensity (Σ). The solid curves are best fits with the activation energy parameters included in the panel. The PL measurements were conducted at 405 nm excitation using a cw laser.

to V1 (at least L1), or similar to V1′ (at least L3). In short, despite the data scattering, we find ample arguments suggesting that the L- and V-lines arise from the same SPE — the V_{Si}.

Having established the strong likelihood of a common origin for the V- and L-lines, we return to the question of how the L-lines arise. V_{Si}^- introduces a set of defect-related orbitals into the 4H-SiC band gap: one a_1 state that is resonant with the valence band, an a_1 orbital containing one electron in the gap, and a degenerate e-state that is doubly occupied and slightly higher in energy than the a_1 gap-state. The ground state (GS) of V_{Si}^- exhibits spin-3/2 and organizes as the $^4A_2$ quartet state with $a_1^2 a_1^1 e^2$ electronic configuration. Correspondingly, the excited states (ES) organize as $^4A_2$ with $a_1^1 a_1^2 e^2$ ordering for V1 and V2, and ^4E with $a_1^1 a_1^1 e^3$ electronic occupation for V1′ and V2′ [11,12,34]. Hence, the V-lines are caused by the promotion of a spin-down electron from the valence band edge to either a_1- (V1 and V2) or e-type (V1′ and V2′) defect orbitals within the band gap (see Supplemental Material at [40] for a schematic diagram of the V_{Si}^- single-particle states). As there are no known additional (spin-conserving) electronic excited state transitions for V_{Si}^-, and close-lying ZPLs from other V_{Si} charge states have not been theoretically predicted and are deemed unlikely, we must search for other explanations. Immediately, the regular and periodic appearance of the L-lines brings to mind the possible involvement of phonons in the optical transitions.

A potential vibrational origin for the family of L-lines resonates well with their observed broadening at elevated temperatures and disappearance above 110 K (see Fig. 4a). Although the V-lines remain visible up to room temperature, phonon-related phenomena are likely to become indistinguishable at lower temperatures than where the original features themselves disappear. Moreover, different vibrational modes would not be expected to respond identically to electric field perturbations (see Fig. 2), and could exhibit varying responses to changes in excitation energy.

A. Vibrational modeling

Let us first consider the possibility of the L-lines originating from conventional vibronic effects related to lattice vibrations. Figure 5(a) illustrates a conceptual configuration coordinate (CC) diagram [45,46] for a transition between the excited state (ES) and ground state (GS) of an arbitrary defect. The diagram thus applies to, e.g., both the V1 and V1′ emission lines. The y-axis denotes energy, with the configuration coordinate Q on the x-axis representing the atomic displacement from the equilibrium position Q_{GS}. The horizontal dashed lines correspond to *vibronic excitations* to each quantum state, of energy spacing $\hbar\omega_{\mathrm{GS}}$ or $\hbar\omega_{\mathrm{ES}}$. The optical transitions absorption and emission occur on a timescale too short for the atomic positions (as represented by the configuration coordinate Q) to rearrange, and are hence vertical in the CC diagram. Upon excitation from the GS (lower parabola in Fig. 5a), the system absorbs a photon of energy $h\nu_{\mathrm{abs}}$ and is transferred to an excited vibronic state of the upper parabola, where energy is exchanged with the lattice to enable reconfiguration towards Q_{ES}. Although absorption and emission take place on the femtosecond timescale, the excited state lifetime can exceed the time of the transition process itself. For example, the excited state PL lifetime of the V_{Si}^- was estimated at $\tau = 6.1$ ns [47]. When the system eventually relaxes towards the ground state, luminescence oc-

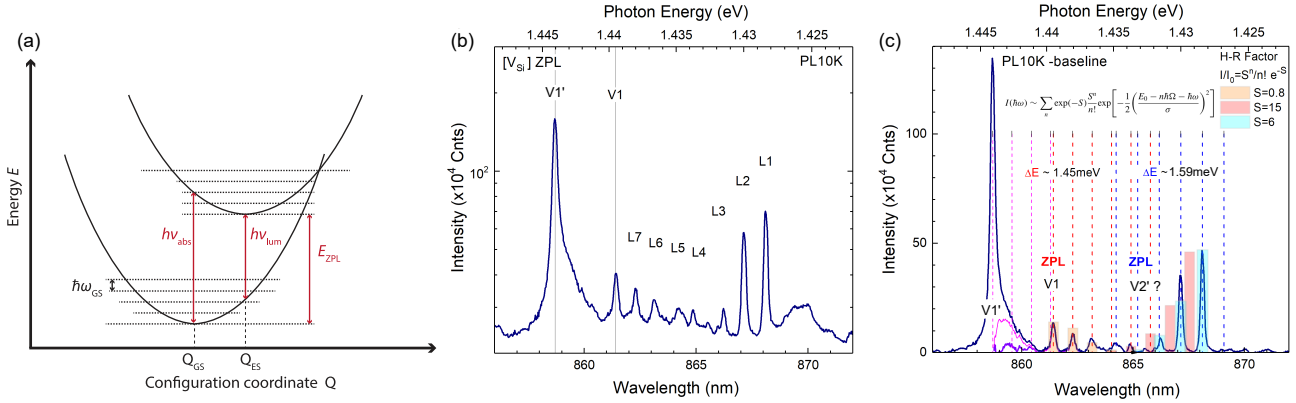

FIG. 5. (a) Conceptual configuration coordinate (CC) diagram for an arbitrary optical transition. (b) PL spectrum from a He-implanted (2.7 MeV) sample, before and (c) after subtracting the background emission. In panel (c), the periodic nature of the emission lines is evidenced by color-coded sets of equidistantly spaced vertical markers. The shaded columns are first-approximations for a given Huang-Rhys factor S. The pink and red lines mark the theorized presence of zero-phonon lines (ZPLs) coinciding with V1′ and V1, respectively, with satellites having 1.45 meV spacing. Blue dashed lines indicate the presence of a ZPL at 1.433 eV with replica spacing of 1.59 meV. Assuming two different ΔE, we put forward a hypothesis for V2′ ZPL positioning at 1.433 eV. The PL spectra were obtained at 10 K using a 405 nm cw laser as an excitation source.

curs in the form of a photon of energy $h\nu_{\rm lum}$, and the system may again interact with the lattice to reoccupy $Q_{\rm GS}$. Such a model would explain the presence of several closely spaced satellites related to the V1 and V1′ zero-phonon lines. It is here important to note that the energy spacing of the L-peaks is reminiscent of the energy scale predicted by density functional theory calculations for comparable defect centers based on a CC diagram perspective — see, e.g., Refs. [32,48] for the case of quantum centers in diamond, and Ref. [12] for that of $V_{\rm Si}$ in 4H-SiC.

Figure 5(b) presents a typical PL spectrum with multi-peak structure on the low-energy side of the V1′/V1 lines. A provisional nomenclature of the emission lines, labeled from right-to-left as L1 through L7, relies on the experimental fact that L1 is the most intense and ever-present feature, while the other lines may appear less distinguishable from the background emission in some spectra. In Figure 5(c), the PL data is plotted on a linear scale with the background emission subtracted, and the periodic nature of the L1-L7 emission lines is evidenced by equidistantly spaced markers (vertical dashed lines). Once the markers are superimposed over the spectra, the existence of two distinct subsets of different line periodicity becomes apparent. Note that the energy separation (ΔE) between adjacent peaks is different for the line groups V1-L4 and L1-L3, i.e., $\sim$1.45 meV and $\sim$1.59 meV, respectively, setting these two groups apart. Such seemingly minor ΔE dissimilarity is nonetheless sufficient for unambiguously setting apart two oscillatory subsets, due to the high precision of energy estimation ensured by the periodicity of the peaks. The L-line spacings ΔE are extracted directly from the PL spectra and are not based on any prior assumptions regarding the origin of the L-lines. It is important to note that while the occurrence of sharp PL lines upon irradiation is common to different SiC polytypes and well documented in the literature [49–52], such a short-period line series has not been reported so far to our knowledge.

Assuming a vibrational nature for the L-lines, the extrapolation of the vertical marker subsets to higher energies predicts potential ZPL positions. Interestingly, the two dominant features in this spectral range — the $V_{\rm Si}$-related V1 and V1′ lines — do coincide with the marker positions (Fig. 5c), suggesting that V1 and V1' act as ZPLs and are at least partly responsible for the L-lines. The color-coded vertical marker sets in Fig. 5(c) indicate three possible starting positions, the first two coinciding with V1′ (magenta) and V1 (red), whereas the third one at 1.443 eV (blue) has no apparent spectral feature behind. Taking into account the dissimilar periodicity and envelope (shape) of the multi-peak subsets, we attempt to model the spectral features assuming vibronic interactions.

The optical transitions that involve vibronic modes are

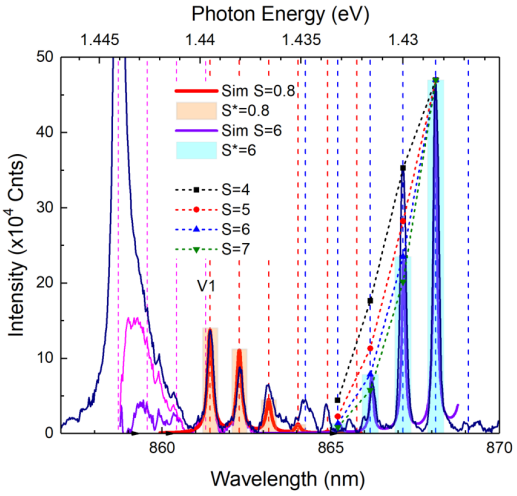

FIG. 6. PL spectrum illustrating HR modeling of the L-lines. The shaded columns are HR first-approximations for a given factor S, and the solid lines represent best fits using full-scale numerical simulation. The PL measurements were obtained at 10 K using a 405 nm cw laser as an excitation source.

commonly modeled using the Huang-Rhys (HR) factor S as a measure of electron-phonon (e-ph) coupling strength [53]. The shaded columns behind the spectral lines in Fig. 5(c) represent a first-approximation (Poisson distribution) of such e-ph coupling described by $I/I_0 = S^n/n!\ e^{-S}$. In the Huang-Rhys scheme, the number (S) and envelope (shape) of the peaks unambiguously specify the position of the ZPL, which in turn may provide insights into the origins of the luminescent centers. Assuming a vibrational nature for the L-lines, a potential model (following a common HR simulation approach [54]) is contained in Figure 6. We infer three independent ZPL subsets, as outlined in Fig. 5(c): ZPL0 (V1′) in magenta, ZPL1 (V1) in red, and ZPL2 (at 1.433 eV) in blue. The vibronic energies are the same for the ZPL0 and ZPL1 subsets (1.45 meV), whereas the ZPL2 (blue) subset has a larger separation energy of 1.59 meV. For the ZPL0 subset, the HR factor cannot be established with certainty due to low intensity of the satellite peaks; however, there are all indications that $S < 1$. The fitting of the ZPL1 (red) subset associated with V1 suggests $S = 0.8$, whereas the ZPL2 (1.433 eV) subset is best characterized by moderate electron-phonon coupling and $S \sim 6$. Numerical details and alternative modeling parameters are presented and discussed in the Supplemental Material at [40].

Provided that the L1-L3 peaks are vibronic replicas of ZPL2 at 1.433 eV (see Fig. 5c and the Supplemental Material at [40] for illustration), there are still ample arguments that all the L-lines originate from the Si vacancy. Interestingly, Ref. [13] proposed that the V2′ ZPL, attributed to the second excited state of $V_{\mathrm{Si}}^{-}(k)$, would occur in close proximity to V1. Hence, we may here speculate that the weak proposed ZPL2 at 1.433 eV in Fig. 5(c) and Fig. 6 is, in fact, the hitherto undetected V2′, as labeled with a question mark in Fig. 5(c). From the (often) weak appearance of V2 and its overlap with the broad phonon side-band of V_{Si}-related emission, we conjecture that the electron-phonon coupling could be stronger for the V2/V2′ lines than that for V1/V1′. Indeed, in such a case of moderate to strong electron-phonon coupling (see Fig. 6), the ZPL could be almost invisible with the phonon satellites being more prominent. Contrarily, weaker coupling to the environment in the case of V1 and V1′ could render the vibronic replicas less prominent than their zero-phonon origins.

Returning to the thermal evolution of the NIR peaks in Fig. 4(b), we now recognize that the existence of two groups of lines following different types of temperature behavior — i.e., clearly exhibit TQ and NTQ features — is reminiscent of similar behavior known for the recombination of excitons bound to neutral and ionized-state impurities (e.g., donor-bound excitons D^0X and D^+X in ZnO [55,56] exhibit TQ and NTQ behavior, respectively). In this regard, the NTQ feature (thermal activation of emission intensity at the outset) is a unique characteristic of the V1′-L3 subset. The TQ process, on the other hand, is controlled by a non-radiative recombination mechanism common to the entire SiC medium (related to the C vacancy and other non-radiative centers), which is apparent from the similarity of the TQ parameters for all lines to that of the integrated (total) PL intensity (Σ-curve in Fig. 4b). This assumption can be verified by referring to the fact that there is a direct relation between thermal activation for quenching and the Huang-Rhys factor [57]. In fact, the activation energy for thermal quenching (E_{A}) can be estimated from the relationship $E_{\mathrm{A}} = (E_0 - E_{\mathrm{R}})^2/4E_{\mathrm{R}}$, where E_0 is the ZPL energy and the relaxation energy is given by $E_{\mathrm{R}} = Sh\Omega$. Referring to the parameters presented in Fig. 5(c) (and the Supplemental Material [40]), a rough E_{A} estimate for the given S range $(6, 15)$ yields E_{A} values well above the experimentally observed $\sim$ 20-70 meV range, thus supporting a common TQ mechanism for all sharp lines and the integrated PL intensity.

B. Dynamic Jahn-Teller effect

Above, the L-lines are tentatively attributed to vibronic replicas of emission from the negatively charged Si vacancy. However, it is important to note that the energy separation between neighboring peaks is around 1.5 meV, which is considerably smaller than the lowest phonon energy observable in 4H-SiC by PL or Raman spectroscopy, with TA = 36 meV [58] and FTA = 24 meV [59] (TA denotes transverse acoustic and FTA zone-folded transverse acoustic phonon modes). Furthermore, recent theoretical studies reinforce this observation, estimating the closest local vibrational modes to the V1 and V2 zero-phonon lines at approximately 30-35 meV [14,33]. In other words, despite the fact that HR modeling nicely captures the periodicity and shape of the L-line spectrum, phonon replicas alone cannot explain the appearance of the L-lines. Referring to reported measurements in SiC and other materials, transitions on the 1 meV energy scale are rare, but observable. Indeed, rotations, or rotational excitations to specific vibrational states, have been detected using infrared spectroscopy in several materials (examples include rotation of an OH-Li center in MgO [60] and H_2 bonds in Si [61,62]). However, as the L-lines are assigned to V_{Si} and because both H and He irradiation are found to induce the L-signals, rotations resulting from molecular and impurity involvement are unlikely to provide an explanation. However, if molecular bonds are not involved, what physical effect may induce rotation-like excitations to the vibronic excited states in Fig. 5(a)? A potential explanation for the L-lines may be uncovered by considering the divacancy (V2) in silicon. In that case, electron paramagnetic resonance (EPR) studies revealed electronic bond switching behavior, which can also be interpreted as a rotation of distortion surrounding the defect center. The bond switching distortion is a thermally activated process, starting at 30 K and with an activation energy of 60 meV [63,64]. No atomic movement is involved, and instead a redistribution of the electron cloud occurs. Intriguingly, the driving force behind such a rotation of distortion was attributed to a dynamic Jahn-Teller (JT) effect arising from coupling between electronic and vibronic states.

A more comparable system to the negatively charged Si vacancy in 4H-SiC is the negative nitrogen-vacancy (NV) center in diamond. In that case, studying the temperature dependence of the PL emission polarization indicated that the dynamic JT effect was the dominant dephasing mech-

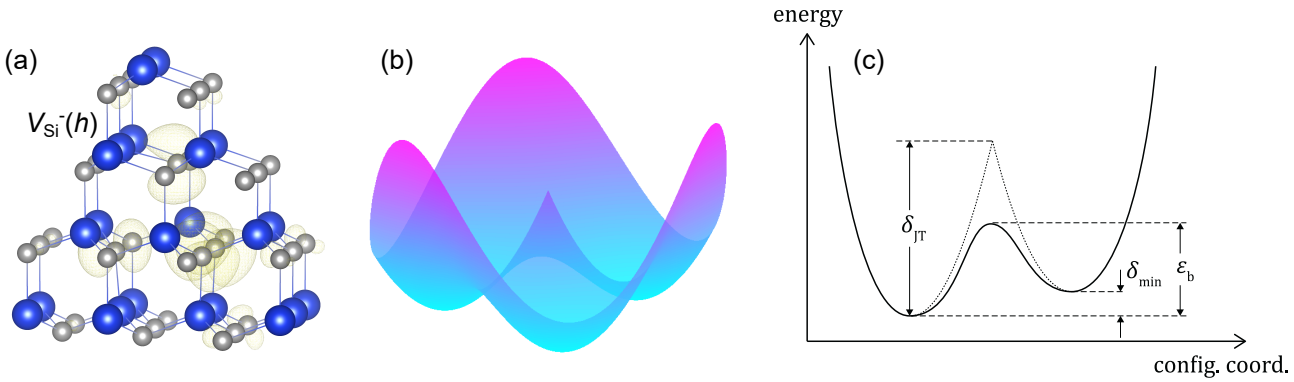

FIG. 7. (a) Geometry and symmetry of the negatively charged Si vacancy at a hexagonal (h) lattice site. (b) Example of the energy distribution associated with the dynamic Jahn-Teller distortion of defect states, in three and (c) two dimensions. The energy lowering is represented by the combination of the δ_{JT}, ε_b, and δ_{min} parameters in panel (c), so that δ_{min} translates to the energy difference between different minima in panel (b).

anism for NV center optical transition [65]. Indeed, the excited state of NV^- is orbitally degenerate, and should therefore experience either a static or dynamic JT effect [66]. A subsequent theoretical work [67] confirmed the dynamic Jahn-Teller effect as being responsible for the observed temperature dependence. Furthermore, by calculating the adiabatic potential energy surface (APES) for NV^-, Ref. [67] found three minima, having an energy δ_{JT} below that of the undistorted structure and separated by a barrier energy ε_b. For NV^- the JT lowering energy was estimated at $\delta_{JT} = 25$ meV, with the three identical local minima being separated by $\varepsilon_b = 10$ meV. The rather small JT energy was attributed to the stiff diamond lattice, a hypothesis that may be valid in SiC as well. Additionally, the low barrier energy (10 meV) would enable rotation between identical structures, and tunneling between the three local minima was predicted to yield a splitting between vibronic excited states. Such a splitting effect (at 11 meV) was, in fact, previously observed experimentally in diamond absorption spectra [68].

From the perspective of attaining stable single-photon emission with high purity suitable for, e.g., spin-photon entanglement and cryptography applications, the presence of a dynamic JT effect is important, as it may diminish the response of defect states to external perturbations such as stress and electric fields. Furthermore, the dynamic JT effect may even dampen the spin-orbit interaction, as theoretically shown in Ref. [69], which may in turn extend spin coherence times of single electron spins trapped at, e.g., NV^- and corresponding qubit centers. Inter-system crossing rates are also affected. An additional example can be found in silicon, where Ref. [70] recently identified new SPEs in the telecom range. Among them is a defect center labeled SD-2, the ZPL of which is always split into three portions separated by 3 meV. This separation was attributed to three different defect configurations being responsible for the emission, which made the ZPL-set less sensitive to strain fluctuations.

Figure 7(a) contains a schematic illustration of $V_{Si}^{-}(h)$ in 4H-SiC, and demonstrates the C_{3v} symmetry taken on by V_{Si} defects. The V1′ and V2′ excited states exhibit orbital degeneracy, while V1 and V2 do not. However, coupling between electronic and vibronic states may lift the stringent degeneracy requirement for JT distortions to occur, in the case that the defect orbitals are sufficiently close in energy. Importantly, several works point towards the potential for a dynamic or motional Jahn-Teller effect in the case of V_{Si} in 4H-SiC. In Ref. [36], a magnetic Jahn-Teller effect was reported for the neutral V_{Si} in 4H-SiC, where the geometry of the atoms was kept fixed, but the symmetry of the dangling bond orbitals was shifted. Unusual temperature dependencies for the coherence times of V_{Si}^{-} centers in 4H-SiC were found in Ref. [35]. Similar trends have been observed for both the divacancy [71] and carbon vacancy [72] in 4H-SiC, and were attributed to motional Jahn-Teller effects in all three cases. Moreover, Ref. [16] predicted inter-level phonon coupling (pseudo-JT effect) between the V1 and V1′ states of V_{Si}^{-}, mediated by the E-symmetry vibrational normal modes of the lattice, and — finally — JT distortions were predicted in the V_{Si} excited states [12].

In accordance with all considerations above, we propose a model for the origin of the L-lines. The degeneracy of the V_{Si}^{-} ground and/or excited states is lifted by a dynamic Jahn-Teller distortion, mediated by moderate electron-phonon coupling. The APES accordingly transforms from one to more minima, for instance three (in the case of nonzero quadratic coupling), as schematically illustrated in Figure 7(b). To account for the close-lying and periodically spaced emission lines (see Fig. 5c), the minima cannot be identical (as proposed for NV^- in diamond [67]), but instead separated by some small energy around 1.5 meV. Figure 7(c) illustrates the cross-section view of the APES in this case, with the periodicity of the L-lines arising from the difference between ε_b and δ_{min}. To account for the two subsets of different line periodicities (1.45 meV and 1.59 meV), we speculate that V_{Si} at both hexagonal and pseudo-cubic lattice sites are responsible for the groups of the L-lines.

Comparing to the alternative vibrational model for the L-lines based on a Huang-Rhys simulation approach, a JT-based explanation appears to better capture the full scope of L-line behavior — not least because phonon modes are unlikely to arise at such short energy scales. Interestingly,

both the Huang-Rhys and JT models group L1 and L2 together based on belonging to the same spacing subset (1.59 meV), in contrast to the experimental observations that sub-divide the two emission lines. However, in the case of both models, the symmetry of the vibronic excitation (in other words, rotation of distortion) yielding each specific L-line would potentially be different. Thus, each vibronic sub-excited state could provide different coupling to electric fields and exhibit separate thermal quenching behavior, much like that of V1 and V1′. Similar observations could explain the varying responses to excitation wavelength. Thus, the interpretation of the different periodicity subsets arising from V_{Si} at h and k lattice sites is reinforced.

Revisiting the experimental findings of this work in light of the JT-based model, we consider the dependence of the L-lines on excitation energy and electric fields. Importantly, both the V- and L-lines exhibit a strong dependence on excitation energy. This can be deduced from Fig. 1, where the ratio of V1:V1′ and the relative intensity difference between L1/L2 and V1/V1′ both depend on the excitation energy (740 nm excitation is used in Figs. 1a and 1b, 405 nm in Fig. 1c). Different excited state symmetries and vibronic coupling could explain these features, but the effect of such an influence remains an open question.

We study two different electric field dependencies using the SBD geometry herein: Stark shift (Fig. 2a) and intensity modulation (Fig. 2b). The intensity modulation with applied bias is similar for the L1, L2 and V1′ [23] lines, supporting the JT hypothesis. The dependencies of the wavelengths of L1 and L2 on the electric field are different, establishing a difference between the L1 and L2 electronic structures. These differences could be attributed to different origins for L1 and L2, or be explained by the JT hypothesis. Indeed, different Stark tuning behaviors were also found for V1 and V1′ in Ref. [24] and attributed to different symmetries and electronic configurations of the excited states. There is a possibility that different symmetries of rotations of distortions driven by the JT effect could explain the different field responses of L1 and L2.

The hypothesis that the hitherto undetected V2′ ZPL may contribute to the zoo of L-lines can, in theory, be verified by correlating the L-line behavior with that of V2. However, the present sample set and measurement geometry did not allow for this comparison on account of the high defect density and resulting overlap between V2 and the broad phonon side-band of the V_{Si} emission. An interesting future study would focus on the V2 line in relation to the L-lines, ideally in samples with a lower overall defect concentration leading to a clearer V2 signal, in order to resolve the remaining questions on how the L-lines arise. Simultaneously, the dependence of the different V- and L-lines on excitation energy should be explored.

The main argument contradicting the vibronic model for L1 and L2 as based on the Huang-Rhys modeling (see, e.g., Fig. 6) is the discrepancy in appearance for L1 and L2. Importantly, L1 and L2 emission intensities exhibit different slopes for the proton fluence dependence (Fig. 1b), and their appearance is not necessarily correlated, although L2 is only observed as companion to L1. While different physical origins may form the explanation for this, one can also conceive that vibronic excited states of different symmetries can respond differently to excitation and local fluctuations. Certainly, more detailed and focused study is needed to elucidate the complex interplay between the Si vacancy electronic states and its environment.

V. CONCLUDING REMARKS

We reveal a set of novel emission lines arising in the near-infrared portion of PL spectra from irradiated n-type 4H-SiC samples, and present strong arguments correlating their origin with the V_{Si}. Among the main arguments suggesting that the L-lines arise from V_{Si}, we point out that the L-lines appear after irradiation using both H and He ions and increase linearly with proton fluence, suggesting correlation with primary irradiation displacements and intrinsic defects — e.g., a vacancy. Similarly with the field dependence of V1′, intensity modulation characteristics for the L1 and L2 lines are observed upon repeatedly biasing the SBD, indicating the occurrence of charge-state switching. Furthermore, the annealing behavior is similar for selected V- and L-lines. Considering the quenching behavior of the V- and L-lines, we find a distinct trend where L1 and V1 exhibit stable thermal quenching, while negative thermal quenching is instead found for L3 and V1′. Thus, we attribute the L1-L7 emission lines to the Si vacancy in 4H-SiC.

The regular periodicity of the L-lines immediately brings to mind phonon involvement, however, local vibrational modes are unlikely to be responsible for the low energy L-line separations of $\sim$1 meV. Instead, although the L-lines can be reliably modeled following a Huang-Rhys simulation approach, we discuss the potential of rotational excitations to the vibronic states giving rise to the L-lines. Indeed, so-called rotations of distortion driven by a dynamic Jahn-Teller effect have been observed for, e.g., the NV center in diamond, and predicted for the V_{Si} in 4H-SiC. Our data, in the context of literature, indicate that the L-lines may be attributed to the fingerprints of the dynamic Jahn-Teller effect for V_{Si} in 4H-SiC. The V1 and V1′ transitions assigned to $V_{\mathrm{Si}}^{-}(h)$ are likely involved in the observed phenomena, and we tentatively suggest that the near-invisible spectral feature at 1.433 eV is related to the hitherto unobserved V2′ excited state of $V_{\mathrm{Si}}^{-}(k)$.

To conclude, we assign the L-lines appearing in the near-infrared portion of PL spectra from irradiated n-type 4H-SiC samples to the vibronic fine-structure of the negatively charged Si vacancy. The driving force behind the L-line emission is likely an electronic bond switching effect, or a rotation of distortion in other words, driven by a dynamic Jahn-Teller effect mediated by electron-phonon coupling.

ACKNOWLEDGMENTS

Financial support was kindly provided by the Research Council of Norway and the University of Oslo through the frontier research project FUNDAMeNT (no. 251131, FriPro ToppForsk-program). The Research Council of

Norway is acknowledged for the support to the Norwegian Micro- and Nano-Fabrication Facility, NorFab, project number 295864. A.D. and V.S. acknowledge AAPSI funding from UVSQ.

[1] N. Iwamoto and B. G. Svensson, Chapter ten - point defects in silicon carbide, in *Defects in Semiconductors*, Semiconductors and Semimetals, Vol. 91, edited by L. Romano, V. Privitera, and C. Jagadish (Elsevier, 2015) pp. 369 – 407.

[2] S. Castelletto, L. Rosa, and B. C. Johnson, Silicon carbide for novel quantum technology devices, in *Advanced Silicon Carbide Devices and Processing* (InTech, 2015).

[3] E. Janzen, A. Gali, P. Carlsson, A. Gallstrom, B. Magnusson, and N. Son, The silicon vacancy in SiC, Physica B: Condensed Matter **404**, 4354 (2009).

[4] M. Widmann, S.-Y. Lee, T. Rendler, N. T. Son, H. Fedder, S. Paik, L.-P. Yang, N. Zhao, S. Yang, I. Booker, A. Denisenko, M. Jamali, S. A. Momenzadeh, I. Gerhardt, T. Ohshima, A. Gali, E. Janzén, and J. Wrachtrup, Coherent control of single spins in silicon carbide at room temperature, Nature Materials **14**, 164 (2014).

[5] S. Castelletto, B. C. Johnson, V. Ivády, N. Stavrias, T. Umeda, A. Gali, and T. Oshima, A silicon carbide room-temperature single-photon source, Nature Materials **13**, 151 (2014).

[6] D. J. Christle, A. L. Falk, P. Andrich, P. V. Klimov, J. U. Hassan, N. T. Son, E. Janzén, T. Oshima, and D. D. Awschalom, Isolated electron spins in silicon carbide with millisecond coherence times, Nature Materials **14**, 160 (2015).

[7] H. J. von Bardeleben, J. L. Cantin, A. Csóré, A. Gali, E. Rauls, and U. Gerstmann, NV centers in 3C, 4H, and 6H silicon carbide: A variable platform for solid-state qubits and nanosensors, Physical Review B **94**, 121202(R) (2016).

[8] T. Bosma, G. J. J. Lof, C. M. Gilardoni, O. V. Zwier, F. Hendriks, B. Magnusson, A. Ellison, A. Gällström, I. G. Ivanov, N. T. Son, R. W. A. Havenith, and C. H. van der Wal, Identification and tunable optical coherent control of transition-metal spins in silicon carbide, npj Quantum Information **4**, 48 (2018).

[9] M. Wagner, B. Magnusson, W. M. Chen, E. Janzén, E. Sörman, C. Hallin, and J. L. Lindström, Electronic structure of the neutral silicon vacancy in 4H and 6H SiC, Physical Review B **62**, 16555 (2000).

[10] E. Sörman, N. T. Son, W. M. Chen, O. Kordina, C. Hallin, and E. Janzén, Silicon vacancy related defect in 4H and 6H SiC, Physical Review B **61**, 2613 (2000).

[11] V. Ivady, J. Davidsson, N. T. Son, T. Ohshima, I. A. Abrikosov, and A. Gali, Identification of Si-vacancy related room-temperature qubits in 4H silicon carbide, Physical Review B **96**, 161114(R) (2017).

[12] P. Udvarhelyi, G. Thiering, N. Morioka, C. Babin, F. Kaiser, D. Lukin, T. Ohshima, J. Ul-Hassan, N. T. Son, J. Vuković, J. Wrachtrup, and A. Gali, Vibronic states and their effect on the temperature and strain dependence of silicon-vacancy qubits in 4H-SiC, Physical Review Applied **13**, 054017 (2020).

[13] M. E. Bathen, L. Vines, and J. Coutinho, First-principles calculations of Stark shifts of electronic transitions for defects in semiconductors: The Si vacancy in 4H-SiC, Journal of Physics: Condensed Matter **33**, 075502 (2020).

[14] A. Hashemi, C. Linderälv, A. V. Karsheninnikov, T. Ala-Nissila, P. Erhart, and H.-P. Komsa, Photoluminescence lineshapes for color centers in silicon carbide from density functional theory calculations (2020).

[15] W. F. Koehl, B. B. Buckley, F. J. Heremans, G. Calusine, and D. D. Awschalom, Room temperature coherent control of defect spin qubits in silicon carbide, Nature **479**, 84 (2011).

[16] R. Nagy, M. Widmann, M. Niethammer, D. B. R. Dasari, I. Gerhardt, Ö. O. Soykal, M. Radulaski, T. Oshima, J. Vucković, N. T. Son, I. G. Ivanov, S. E. Economou, C. Bonato, S.-Y. Lee, and J. Wrachtrup, Quantum properties of dichroic silicon vacancies in silicon carbide, Physical Review Applied **9**, 034022 (2018).

[17] R. Nagy, M. Niethammer, M. Widmann, Y.-C. Chen, P. Udvarhelyi, C. Bonato, J. U. Hassan, R. Karhu, I. G. Ivanov, N. T. Son, J. R. Maze, T. Oshima, Ö. O. Soykal, A. Galí, S.-Y. Lee, F. Kaiser, and J. Wrachtrup, High-fidelity spin and optical control of single silicon-vacancy centres in silicon carbide, Nature Communications **10**, 1054 (2019).

[18] M. E. Bathen and L. Vines, Manipulating single-photon emission from point defects in diamond and silicon carbide, Advanced Quantum Technologies , 2100003 (2021).

[19] H. Kraus, D. Simin, C. Kasper, Y. Suda, S. Kawabata, W. Kada, T. Honda, Y. Hijikata, T. Ohshima, V. Dyakonov, and G. V. Astakhov, Three-dimensional proton beam writing of optically active coherent vacancy spins in silicon carbide, Nano Letters **17**, 2865 (2017).

[20] J. Wang, Y. Zhou, X. Zhang, F. Liu, Y. Li, K. Li, Z. Liu, G. Wang, and W. Gao, Efficient generation of an array of single silicon-vacancy defects in silicon carbide, Physical Review Applied **7**, 064021 (2017).

[21] J. Wang, X. Zhang, Y. Zhou, K. Li, Z. Wang, P. Peddibhotla, F. Liu, S. Bauerdick, A. Rudzinski, Z. Liu, and W. Gao, Scalable fabrication of single silicon vacancy defect arrays in silicon carbide using focused ion beam, ACS Photonics **4**, 1054 (2017).

[22] S. Castelletto, B. C. Johnson, and A. Boretti, Visible and infrared photoluminescence in hexagonal silicon carbide by direct femtosecond laser writing, IOP Conf. Ser.: Mater. Sci. Eng. **840**, 012010 (2020).

[23] M. E. Bathen, A. Galeckas, J. Müting, H. M. Ayedh, U. Grossner, J. Coutinho, Y. K. Frodason, and L. Vines, Electrical charge state identification and control for the silicon vacancy in 4H-SiC, npj Quantum Information **5**, 111 (2019).

[24] M. Rühl, L. Bergmann, M. Krieger, and H. B. Weber, Stark tuning of the silicon vacancy in silicon carbide, Nano Letters **20**, 658 (2020).

[25] D. M. Lukin, A. D. White, R. Trivedi, M. A. Guidry, N. Morioka, C. Babin, Ö. O. Soykal, J. Ul Hassan, N. T. Son, T. Ohshima, P. K. Vasireddy, M. H. Nasr, S. Sun, J.-P. W. Maclean, C. Dory, E. A. Nanni, J. Wrachtrup, F. Kaiser, and J. Vuckovic, Spectrally reconfigurable quantum emitters enabled by optimized fast modulation, npj Quantum Information **6**, 80 (2020).

[26] C. F. de la Casas, D. J. Christle, J. Ul Hassan, T. Ohshima, N. T. Son, and D. D. Awschalom, Stark tuning and electrical charge state control of single divacancies in silicon carbide, Applied Physics Letters **111**, 262403 (2017).

[27] C. P. Anderson, A. Bourassa, K. C. Miao, G. Wolfowicz, P. J. Mintun, A. L. Crook, H. Abe, J. Ul Hassan, N. T. Son, T. Oshima, and D. D. Awschalom, Electrical and optical control of single spins integrated in scalable semiconductor

devices, Science **366**, 1225 (2019).
[28] K. C. Miao, A. Bourassa, C. P. Anderson, S. J. Whiteley, A. L. Crook, S. L. Bayliss, G. Wolfowicz, G. Thiering, P. Udvarhelyi, V. Ivády, H. Abe, T. Ohshima, A. Gali, and D. D. Awschalom, Electrically driven optical interferometry with spins in silicon carbide, Science Advances **5**, eaay0527 (2019).
[29] J. Stark, Beobachtungen über den Effekt des elektrischen Feldes auf Spektrallinien i. Quereffekt, Annalen der Physik **50**, 489 (1914).
[30] C. G. Vásquez, M. E. Bathen, A. Galeckas, C. Bazioti, K. M. Johansen, D. Maestre, A. Cremades, Ø. Prytz, A. M. Moe, A. Yu. Kuznetsov, and L. Vines, Strain modulation of Si vacancy quantum emission from SiC micro- and nanoparticles, Nano Letters **20**, 8689 (2020).
[31] A. Gali, E. Janzén, P. Deák, G. Kresse, and E. Kaxiras, Theory of spin-conserving excitation of the NV center in diamond, Physical Review Letters **103**, 186404 (2009).
[32] A. Alkauskas, B. B. Buckley, D. D. Awschalom, and C. G. Van de Walle, First-principles theory of the luminescence lineshape for the triplet transition in diamond NV centres, New J. Phys. **16**, 073026 (2014).
[33] Z. Shang, A. Hashemi, Y. Berencen, H.-P. Komsa, P. Erhart, S. Zhou, M. Helm, A. V. Krasheninnikov, and G. V. Astakhov, Local vibrational modes of Si vacancy spin qubits in SiC, Physical Review B **101**, 144109 (2020).
[34] A. Gali, Excitation properties of silicon vacancy in silicon carbide, Materials Science Forum **717–720**, 255 (2012).
[35] J. S. Embley, J. S. Colton, K. G. Miller, M. A. Morris, M. Meehan, S. L. Crossen, B. D. Weaver, E. R. Glaser, and S. G. Carter, Electron spin coherence of silicon vacancies in proton-irradiated 4H-SiC, Physical Review B **95**, 045206 (2017).
[36] A. Zywietz, J. Furthmüller, and F. Bechstedt, Spin state of vacancies: From magnetic Jahn-Teller distortions to multiplets, Physical Review B **62**, 6854 (2000).
[37] J. W. Steeds, Photoluminescence study of the carbon antisite-vacancy pair in 4H- and 6H-SiC, Physical Review B **80**, 245202 (2009).
[38] M. Rühl, C. Ott, S. Gätzinger, M. Krieger, and H. B. Weber, Controlled generation of intrinsic near-infrared color centers in 4H-SiC via proton irradiation and annealing, Applied Physics Letters **113**, 122102 (2018).
[39] J. F. Ziegler, M. Ziegler, and J. Biersack, SRIM – the stopping and range of ions in matter (2010), Nuclear Instruments and Methods in Physics Research Section B: Beam Interactions with Materials and Atoms **268**, 1818 (2010).
[40] Supplemental Material (2021).
[41] M. E. Bathen, A. Galeckas, J. Coutinho, and L. Vines, Influence of hydrogen implantation on emission from the silicon vacancy in 4H-SiC, Journal of Applied Physics **127**, 085701 (2020).
[42] M. Widmann, M. Niethammer, D. Y. Fedyanin, I. A. Khramtsov, T. Rendler, I. D. Booker, J. U. Hassan, N. Morioka, Y.-C. Chen, I. G. Ivanov, N. T. Son, T. Ohshima, M. Bockstedte, A. Gali, C. Bonato, S.-Y. Lee, and J. Wrachtrup, Electrical charge state manipulation of single silicon vacancies in a silicon carbide quantum optoelectronic device, Nano Letters **19**, 7173 (2019).
[43] T. Hornos, A. Gali, and B. G. Svensson, Large-scale electronic structure calculations of vacancies in 4H-SiC using the Heyd-Scuseria-Ernzerhof screened hybrid density functional, Materials Science Forum **679-680**, 261 (2011).
[44] R. M. Karsthof, M. E. Bathen, A. Galeckas, and L. Vines, Conversion pathways of primary defects by annealing in proton-irradiated n-type 4H-SiC, Physical Review B **102**, 184111 (2020).
[45] I. Pelant and J. Valenta, *Luminescence Spectroscopy of Semiconductors* (Oxford Scholarship Online, 2012).
[46] C. Freysoldt, B. Grabowski, T. Hickel, J. Neugebauer, G. Kresse, A. Janotti, and C. G. van de Walle, First-principles calculations for point defects in solids, Reviews of Modern Physics **86**, 253 (2014).
[47] T. C. Hain, F. Fuchs, V. A. Soltamov, P. G. Baranov, G. V. Astakhov, T. Hertel, and V. Dyakonov, Excitation and recombination dynamics of vacancy-related spin centers in silicon carbide, Journal of Applied Physics **115**, 133508 (2014).
[48] E. Londero, G. Thiering, L. Razinkovas, A. Gali, and A. Alkauskas, Vibrational modes of negatively charged silicon-vacancy centers in diamond from *ab initio* calculations, Physical Review B **98**, 035306 (2018).
[49] W. J. Choyke and L. Patrick, Photoluminescence of radiation defects in cubic SiC: Localized modes and Jahn-Teller effect, Physical Review B **4**, 1843 (1971).
[50] L. Patrick and W. J. Choyke, Photoluminescence of radiation defects in ion-implanted 6H-SiC, Physical Review B **5**, 3253 (1972).
[51] H. Itoh, M. Yoshikawa, I. Nashiyama, H. Okumura, S. Misawa, and S. Yoshida, Photoluminescence of radiation induced defects in 3C-SiC epitaxially grown on Si, Journal of Applied Physics **77**, 837 (1995).
[52] T. Egilsson, A. Henry, I. G. Ivanov, J. L. Lindström, and E. Janzén, Photoluminescence of electron-irradiated 4H-SiC, Physical Review B **59**, 8008 (1999).
[53] K. Huang and A. Rhys, Theory of light absorption and nonradiative transitions in F-centres, Proc. R. Soc. Lond. A **204**, 406 (1950).
[54] C. Spindler, F. Babbe, M. H. Wolter, F. Ehre, K. Santhosh, P. Hilgert, F. Werner, and S. Siebentritt, Electronic defects in Cu(In,Ga)Se_2: Towards a comprehensive model, Physical Review Materials **3**, 090302 (2019).
[55] B. K. Meyer, J. Sann, S. Eisermann, S. Lautenschlaeger, M. R. Wagner, M. Kaiser, G. Callsen, J. S. Reparaz, and A. Hoffmann, Excited state properties of donor bound excitons in ZnO, Physical Review B **82**, 115207 (2010).
[56] R. J. Mendelsberg, M. W. Allen, S. M. Durbin, and R. J. Reeves, Photoluminescence and the exciton-phonon coupling in hydrothermally grown ZnO, Physical Review B **83**, 205202 (2011).
[57] A. Alkauskas, M. D. McCluskey, and C. G. Van de Walle, Tutorial: Defects in Semiconductors - Combining experiment and theory, Journal of Applied Physics **119**, 181101 (2016).
[58] J. A. Freitas Jr., Properties of silicon carbide (INSPEC, the Institution of Electrical Engineers, 1995) Chap. Photoluminescence spectra of SiC polytypes, pp. 29–41.
[59] S. Nakashima and H. Harima, Raman investigation of SiC polytypes, physica status solidi (a) **162**, 39 (1997).
[60] K. R. Martin, C. Peng, S. Kleekajai, P. Blaney, E. Diamond, W. B. Fowler, M. Stavola, and R. González, Hindered rotation of an OH-Li center in MgO: Infrared absorption experiments and theory, Physical Review B **75**, 245211 (2007).
[61] E. E. Chen, M. Stavola, and W. B. Fowler, Ortho and para O-H_2 complexes in silicon, Physical Review B **65**, 245208 (2002).
[62] E. E. Chen, M. Stavola, W. B. Fowler, and P. Walters, Key to understanding interstitial H_2 in Si, Physical Review Letters **88**, 105507 (2002).
[63] G. D. Watkins and J. W. Corbett, Defects in irradiated silicon: Electron paramagnetic resonance and electron-nuclear double resonance of the Si-E center, Physical Review **134**,

1359 (1964).
[64] G. D. Watkins and J. W. Corbett, Defects in irradiated silicon: Electron paramagnetic resonance of the divacancy, Physical Review **138**, 543 (1965).
[65] K.-M. C. Fu, C. Santori, P. E. Barclay, L. J. Rogers, N. B. Manson, and R. G. Beausoleil, Observation of the dynamic Jahn-Teller effect in the excited states of nitrogen-vacancy centers in diamond, Physical Review Letters **103**, 256404 (2009).
[66] H. A. Jahn and E. Teller, Stability of polyatomic molecules in degenerate electronic states - I—Orbital degeneracy, Proceedings of the Royal Society A **161**, 220 (1937).
[67] T. A. Abtew, Y. Y. Sun, B.-C. Shih, P. Dev, S. B. Zhang, and P. Zhang, Dynamic Jahn-Teller effect in the NV^- center in diamond, Physical Review Letters **107**, 146403 (2011).
[68] G. Davies and M. F. Hamer, Optical studies of the 1.945 eV vibronic band in diamond, Proc. R. Soc. Lond. A **348**, 285 (1976).
[69] G. Thiering and A. Gali, Ab initio calculation of spin-orbit coupling for an NV center in diamond exhibiting dynamic Jahn-Teller effect, Physical Review B **96**, 081115(R) (2017).
[70] A. Durand, Y. Baron, W. Redjem, T. Herzig, A. Benali, S. Pezzagna, J. Meijer, A. Y. Kuznetsov, J.-M. Gérard, I. Robert-Philip, M. Abbarchi, V. Jacques, G. Cassabois, and A. Dréau, Broad diversity of near-infrared single-photon emitters in silicon, Physical Review Letters **126**, 083602 (2021).
[71] A. L. Falk, P. V. Klimov, V. Ivády, K. Szász, D. J. Christle, W. F. Koehl, A. Gali, and D. D. Awschalom, Optical polarization of nuclear spins in silicon carbide, Physical Review Letters **114**, 247603 (2015).
[72] T. Umeda, J. Isoya, N. Morishita, T. Ohshima, T. Kamiya, A. Gali, P. Deák, N. T. Son, and E. Janzén, EPR and theoretical studies of positively charged carbon vacancy in 4H-SiC, Physical Review B **70**, 235212 (2004).